

# Design of double- and multi-bend achromat lattices with large dynamic aperture and approximate invariants

Yongjun Li,<sup>1,\*</sup> Kilean Hwang,<sup>2</sup> Chad Mitchell,<sup>2,†</sup> Robert Rainer,<sup>1</sup> Robert Ryne,<sup>2</sup> and Victor Smaluk<sup>1</sup>

<sup>1</sup>*Brookhaven National Laboratory, Upton 11973, New York, USA*

<sup>2</sup>*Lawrence Berkeley National Laboratory, Berkeley 94720, California, USA*

A numerical method to design nonlinear double- and multi-bend achromat (DBA and MBA) lattices with approximate invariants of motion is investigated. The search for such nonlinear lattices is motivated by Fermilab's Integrable Optics Test Accelerator (IOTA), whose design is based on an integrable Hamiltonian system with two invariants of motion. While it may not be possible to design an achromatic lattice for a dedicated synchrotron light source storage ring with one or more exact invariants of motion, it is possible to tune the sextupoles and octupoles in existing DBA and MBA lattices to produce approximate invariants. In our procedure, the lattice is tuned while minimizing the turn-by-turn fluctuations of the Courant-Snyder actions  $J_x$  and  $J_y$  at several distinct amplitudes, while simultaneously minimizing diffusion of the on-energy betatron tunes. The resulting lattices share some important features with integrable ones, such as a large dynamic aperture, trajectories confined to invariant tori, robustness to resonances and errors, and a large amplitude-dependent tune-spread.

## I. INTRODUCTION

The Integrable Optics Test Accelerator (IOTA) [1], whose design is based on an integrable Hamiltonian system with two invariants of motion [2, 3], paves the way for a new class of highly nonlinear storage rings. Experiments using a lattice design with one invariant of motion have also been performed, both at IOTA and in the University of Maryland Electron Ring (UMER) [4]. In each case, the lattice is tuned to provide one or more analytically known invariants of motion, resulting in a dynamic aperture (DA) that is large and robust to the presence of resonances.

The storage rings used as dedicated synchrotron light sources are designed in a different way: a linear achromat lattice with a desired beam emittance is designed first, and then the nonlinear dynamics is optimized with sextupoles and/or octupoles. The nonlinear magnets are often tuned to control the low order resonance driving terms of the one-turn map [5] to obtain sufficient dynamic aperture. Under these conditions it is generally difficult, if not impossible, to optimize the nonlinear dynamics to produce a one-turn map with one or more exact invariants. However, it is sometimes possible to produce approximate invariants, or quasi-invariants (QI), in these achromat lattices. This paper describes a procedure for designing near-integrable double-bend achromat (DBA) and multi-bend achromat (MBA) lattices with two QI. The motivation for constructing such lattices is that, although they are not completely integrable, the DA is large and robust to the presence of resonances. While crossing the resonance lines, their stop-band widths are observed narrow as well. Like nonlinear integrable lattices such as the one at IOTA, these lattices also have a

large amplitude-dependent betatron tune-spread which can increase instability and space charge thresholds due to improved Landau damping [6, 7]. Therefore the requirements on the feedback system's gain could be reduced significantly. This research was motivated by related studies such as the square matrix method [8] and the constant Courant-Snyder invariant method [9, 10].

The remainder of this paper is outlined as follows: Section II explains the concept of Poisson-commuting invariants in integrable Hamiltonian systems, and describes a numerical approach for optimizing the nonlinear lattice to produce approximate invariants using symplectic tracking. Sections III and IV describe the properties of two such lattices, both of which have been constructed: the existing National Synchrotron Light Source-II (NSLS-II) DBA storage ring, and a diffraction-limited MBA storage ring (whose design is preliminary). Some detailed studies of the DBA lattice are described in Sect. V. Section VI describes the simulation of a kicked beam to illustrate the decoherence effect that results from a large nonlinear tune-spread. Some discussion and a brief summary are given in Sect. VII. A technique to modify the action-like invariants to reshape the invariant tori (and the resulting DA) is described in the Appendix.

## II. LATTICE DESIGN PROCEDURE

A Hamiltonian system is *Liouville integrable* if it possesses a maximal set of independent Poisson commuting invariants of motion. For a system described by a symplectic map on a phase space of dimension  $2n$ , this means that there exist  $n$  functions  $f_j$  ( $j = 1, \dots, n$ ) on the phase space such that: i) each  $f_j$  is invariant under the map, ii) the Poisson brackets satisfy  $[f_i, f_j] = 0$ , and iii) the set of gradient vectors  $\{\nabla f_j : j = 1, \dots, n\}$  are linearly independent [11, 12]. The behavior of trajectories for

\* email: yli@bnl.gov

† email: chadmitchell@lbl.gov

a completely integrable system is well-known, i.e., all its trajectories are confined to tori with well-defined and stable tunes.

By ignoring radiation and longitudinal acceleration, a charged particle's transverse motion in a storage ring is a 4-dimensional Hamiltonian system, described by a symplectic one-turn map  $\mathcal{M}$ . If we let the canonical coordinates of the system be denoted  $\mathbf{z} = (x, p_x; y, p_y)$ , a quantity  $f(\mathbf{z})$  is an invariant of the map  $\mathcal{M}$  if:

$$f(\mathcal{M}(\mathbf{z})) = f(\mathbf{z}). \quad (1)$$

If two such invariants  $f_i$ , ( $i = 1, 2$ ) exist, if they are independent:

$$\nabla f_1 \times \nabla f_2 \neq 0, \quad (2)$$

and if they Poisson-commute:

$$\begin{aligned} [f_1, f_2] &= \left( \frac{\partial f_1}{\partial x} \frac{\partial f_2}{\partial p_x} - \frac{\partial f_1}{\partial p_x} \frac{\partial f_2}{\partial x} \right) \\ &+ \left( \frac{\partial f_1}{\partial y} \frac{\partial f_2}{\partial p_y} - \frac{\partial f_1}{\partial p_y} \frac{\partial f_2}{\partial y} \right) = 0, \end{aligned} \quad (3)$$

the lattice is Liouville integrable.

When the map  $\mathcal{M}$  is linear and uncoupled, the Courant-Snyder actions  $J_x$  and  $J_y$  form the most commonly-used Poisson commuting pair of invariants, where:

$$J_x = \frac{1}{2}(\bar{x}^2 + \bar{p}_x^2) = \frac{1}{2}(\gamma_x x^2 + 2\alpha_x x p_x + \beta_x p_x^2), \quad (4)$$

in the horizontal plane, with a similar expression for  $J_y$ . Here, the normalized coordinates  $\bar{x}$  and  $\bar{p}_x$  are given by:

$$\begin{bmatrix} \bar{x} \\ \bar{p}_x \end{bmatrix} = \begin{bmatrix} \frac{1}{\sqrt{\beta_x}} & 0 \\ \frac{\alpha_x}{\sqrt{\beta_x}} & \sqrt{\beta_x} \end{bmatrix} \begin{bmatrix} x \\ p_x \end{bmatrix}, \quad (5)$$

where  $\alpha_x$ ,  $\beta_x$ , and  $\gamma_x$  are the horizontal Twiss parameters [13] at the longitudinal location where the Poincaré section is observed. The canonical action-angle coordinates are  $(\Phi_x, J_x, \Phi_y, J_y)$ , where  $\Phi_{x,y}$  denotes the betatron phase in each plane, and the one-turn map is determined by the phase advance completed in a single revolution:

$$\begin{aligned} \phi_x &= \Phi_{x,i+1} - \Phi_{x,i} \\ &= -\arctan\left(\frac{\bar{p}_{x,i+1}}{\bar{x}_{i+1}}\right) + \arctan\left(\frac{\bar{p}_{x,i}}{\bar{x}_i}\right) + k \cdot 2\pi, \end{aligned}$$

with a similar expression for  $\phi_y$ . Here,  $k$  is the integer part of the betatron tune. The phase advance values  $\phi_x$ ,  $\phi_y$  are independent of the actions  $J_x$  and  $J_y$ .

In a realistic storage ring, once the linear lattice and the nonlinear magnet locations are fixed, the one-turn map  $\mathcal{M}$  depends on the nonlinear magnet strengths  $K_i$ , with  $i \geq 2$ . It is difficult, if not impossible, to tune the  $K_i$  so that  $\mathcal{M}$  possesses even one exact invariant. However, we can imitate the linear case by constructing

a nonlinear system in which the Courant-Snyder actions  $J_x$ ,  $J_y$  form a pair of approximate invariants, as illustrated in Fig. 1. Unlike the linear case, however, the phase advance values  $\phi_x$  and  $\phi_y$  can depend on the actions  $J_x$  and  $J_y$ .

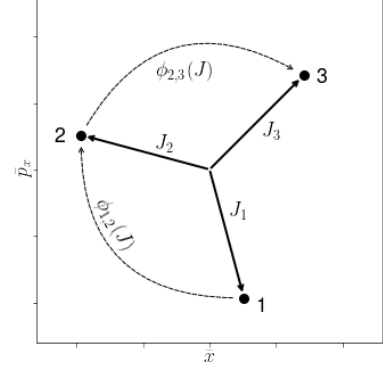


Figure 1. Schematic illustration of a rotating trajectory observed at a Poincaré section with normalized coordinates  $(\bar{x}, \bar{p}_x)$ . The fluctuations of the action  $J_x$  and phase advance  $\phi_x$ , in multi-turn tracking simulations are the objectives to be minimized. A similar picture applied in the vertical plane.

The procedure is as follows. To optimize the behavior of the Courant-Snyder action  $J_x$  within the available DA, multiple particles with different values of  $J_{x,0}$  are launched. Element-by-element tracking of this set of particles is used to compute the turn-by-turn evolution of  $J_x$ . The tracking is implemented with a kick-drift symplectic integrator [14] to preserve the geometry of the Hamiltonian system. The available nonlinear knobs are simultaneously tuned to minimize the turn-by-turn fluctuations of  $J_x$  for each particle, as illustrated in Fig. 2.

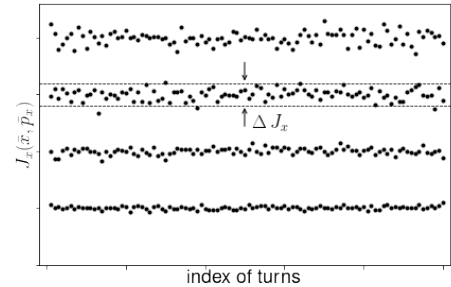


Figure 2. Schematic illustration of the fluctuation of actions  $\Delta J_x$  starting from different initial amplitudes. Usually the fluctuations increase gradually with the initial amplitude.

At the same time, we minimize the turn-to-turn variations of the horizontal phase advance. Instead of directly calculating  $\phi_x$ , the turn-to-turn evolution of  $\bar{x} \pm i\bar{p}_x$  [15] was analyzed in the frequency domain. One reason for using such a spectral method is to determine whether the fractional tune is below or above the half integer. The amplitudes of the two leading frequencies were computed

utilizing the Numerical Analysis of Fundamental Frequencies (NAFF) technique [16]. By tuning the nonlinear knobs, the ratio between the two leading frequencies  $r = \frac{A_2}{A_1}$  was minimized. As a consequence, the smaller amplitude frequencies were also suppressed (Fig. 3). Note that this procedure is performed independently for several initial conditions of varying amplitude. As a result, the tune diffusion of each particle is suppressed, but the tunes may be amplitude-dependent. The same procedure is repeated for the vertical plane.

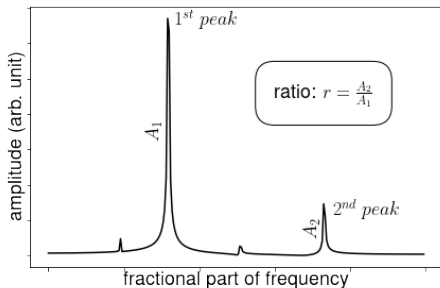


Figure 3. Schematic illustration of the spectrum obtained from turn-by-turn trajectory data  $\bar{x} \pm i\bar{p}_x$ . The ratio between the amplitudes of the two leading frequencies  $\frac{A_2}{A_1}$  is the minimization objective used to minimize the orbit tune diffusion.

Since the goal is to minimize the fluctuations of four different quantities for different initial conditions simultaneously, the construction of such a nonlinear lattice becomes a typical multi-objective optimization problem:

- given a set of nonlinear knobs  $K_i$  within their allowed ranges;
- subject to some constraints, such as maintaining certain desired chromaticities;
- simultaneously minimize the objective functions, i.e.,  $\frac{\Delta J_{x,y}}{J_{x,y}}$  and  $r_{x,y} = \frac{A_{2;x,y}}{A_{1;x,y}}$  of multi-particles launched from different initial conditions.

Multi-objective optimization techniques are widely used in the accelerator community now. Here, the non-dominated sorting genetic algorithm-II [17] was used. For each initial condition, the number of objectives is 4. Usually five virtual particles with gradually increased initial  $J_{0;x,y}$  were launched. The total number of objectives is  $5 \times 4 = 20$ .

Thus far, we have only discussed uncoupled linear lattices. When linear coupling is present, a different parameterization, such as the one described in [18], is needed.

### III. APPLIED TO DOUBLE-BEND ACHROMAT

In this Section, we introduce a nonlinear DBA lattice for the NSLS-II main storage ring [19], which is presently in operation at Brookhaven National Laboratory. It is a

3<sup>rd</sup> generation medium energy (3 GeV) light source. The storage ring's lattice is a typical DBA structure with its main parameters listed in Table I. Its linear optics for one cell is illustrated in Fig. 4. The whole ring is composed of 30 such cells. In this configuration, three families of chromatic sextupoles are used to correct its chromaticity to +7. Then, six families of harmonic sextupoles in dispersion-free sections are used as tuning knobs for the multi-objective optimization described in Section II.

Table I. Main parameters of NSLS-II storage ring

Parameters	Values
Hor. emit. (nm)	2.1
Natural chrom. (x/y)	-101/-40
Tune (x/y)	33.22/16.26
Energy spread	$5.1 \times 10^{-4}$
Damp. partition (x/y/s)	1.0/1.0/2.0

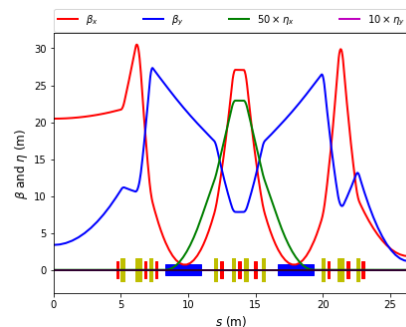


Figure 4. (Color) The linear optics and magnet layout for one cell of the NSLS-II storage ring. The red blocks represent sextupoles. The strengths of six harmonic sextupoles were tuned during optimization of the nonlinear optics (Sect. II).

Below, we present the nonlinear lattice performance of an optimized solution using the tracking simulation code ELEGANT [20]. All the tracking simulations in this paper were performed with this code unless stated otherwise. Figure 5 illustrates the on-momentum DA (through 1,024 turns of particle tracking). Each stable initial condition is colored with the tune diffusion rate (over 1,024 turns) obtained using the NAFF technique.

The turn-by-turn evolution of the Courant-Snyder actions  $J_{x,y}$  for particles at 5 distinct amplitudes are shown in Fig. 6. The size of the visible fluctuations increases gradually with the amplitude of the initial condition. The spectral analysis of tracking data using the NAFF technique indicates that some non-dominant frequencies gradually become stronger as well (Fig. 7). The amplitude ratio between the two leading frequencies increases as shown in Fig. 8.

One of the features of an integrable system is that the trajectories are confined to tori in the phase space. This is apparent in the turn-by-turn tracking data shown in

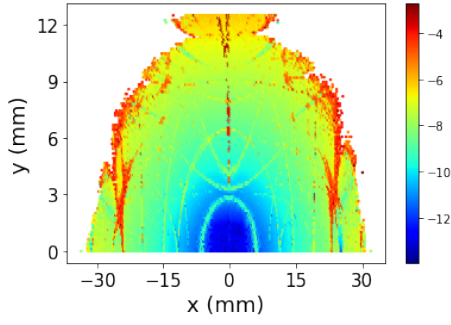


Figure 5. (Color) DA of the DBA lattice observed at the center of long straight section, i.e.,  $s = 0$  in Fig. 4. Colors indicate the tune diffusion rate.

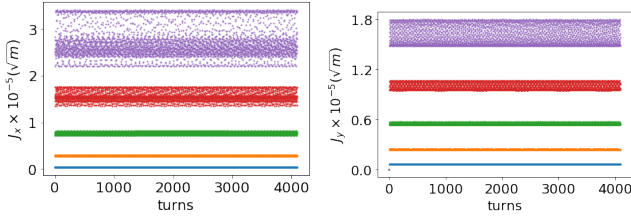


Figure 6. (Color) Evolution of  $J_{x,y}$  in the DBA lattice starting from 5 different initial conditions in the horizontal (left) and vertical (right) planes.

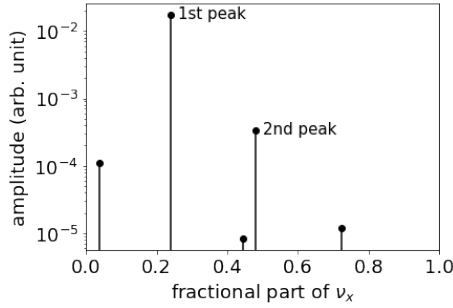


Figure 7. Some leading frequency components extracted from a set of turn-by-turn data  $\bar{x} \pm i\bar{p}_x$  using the NAFF technique for the DBA lattice.

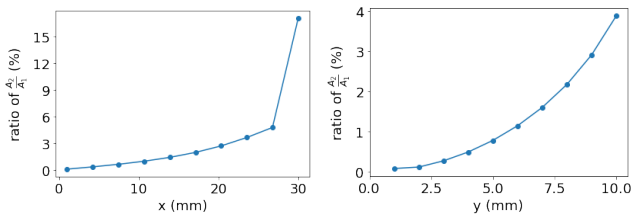


Figure 8. The ratio of the two leading NAFF components increases with the initial particle amplitude in the horizontal (left) and vertical (right) planes for the DBA lattice.

Fig. 9. Although trajectories begin to gradually deviate from the Courant-Snyder ellipse when the amplitude in-

creases, they are still confined to deformed tori. It therefore appears that this lattice possesses two QIs whose values near the reference orbit are quantitatively close to the Courant-Snyder actions.

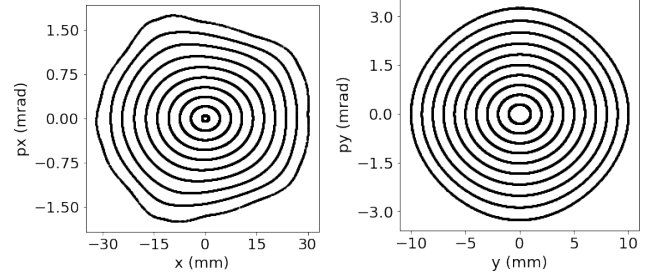


Figure 9. Simulated trajectories of the DBA lattice starting from different initial conditions in the horizontal (left) and vertical (right) phase space. Within the DA, although the trajectories deviate from the Courant-Snyder ellipse, they are still confined to thin tori.

Like the IOTA ring, this lattice also provides a large amplitude-dependent tune-spread as illustrated in Fig. 10. This property can increase instability and space charge thresholds through improved Landau damping. Even while crossing the low order resonance lines such as  $\nu_x = 1/3$ , the stop-band widths are observed quite narrow.

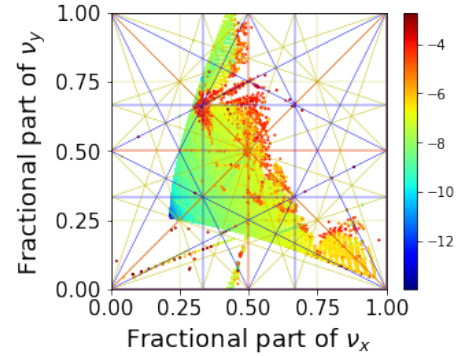


Figure 10. (Color) Tune footprint of the DBA lattice in the tune space. A large amplitude-dependent tune-spread is observed, and various resonance lines can be crossed with narrow stop-band widths.

The robustness of this lattice has been confirmed in both simulation and experiment. After adding various realistic errors on the magnets in the simulation, a sufficient DA for the off-axis injection remains as illustrated in Fig. 11. This lattice has also been successfully commissioned at the NSLS-II ring by modifying its sextupoles settings. A near 100% off-axis injection efficiency was achieved, which indicates its DA is sufficient for routine operation. The DA was also directly measured by kicking a stored beam transversely to observe its loss. Although the measured DA is worse than the simulation prediction, it can satisfy the requirement for the off-axis injection.

After accumulated a beam current up to 400 mA, the bunch-by-bunch feedback system was re-optimized to reduce its gain gradually. Each bunch's turn-by-turn data was used for a spectral analysis to identify the appearance of sidebands of Betatron motion caused by various instabilities. Compared with the nominal NSLS-II lattice, the required gain for this nonlinear lattice can be reduced by 50% and 75% in the horizontal and vertical planes, respectively. This appears to be due to the increase nonlinear tune-spread and chromaticity.

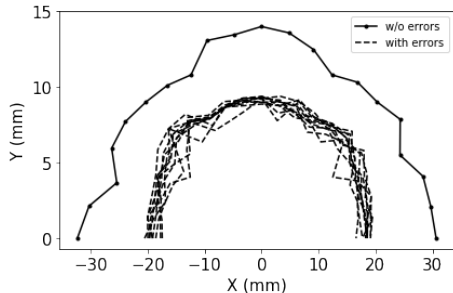


Figure 11. Dynamic apertures of the DBA lattice with QI when realistic magnet multipole errors are included. The solid line represents the DA for a perfect machine. The dashed ones are the DAs with the presence of both the systematic and random multipole errors for 10 random seeds. The needed aperture for off-axis injection is around 11 mm

#### IV. APPLIED TO MULTI-BEND ACHROMAT

Low-emittance light source ring design is now entering a new era. Various MBA-type lattices already reach diffraction-limited horizontal emittances to deliver much brighter X-ray beams. Like the DBA case, it is interesting to explore whether it is possible to design a nonlinear MBA lattice with two QIs. The ESRF-EBS type hybrid MBA lattice [21] has been widely adopted by other facilities. It is also being considered as one of the options for future NSLS-II brightness upgrade. A preliminary 7-BA design is shown in Fig. 12, which illustrates the linear optics for one cell. Note that several reverse bends are incorporated [22, 23]. The main parameters are listed in Table II.

Table II. Main parameters of the test hybrid MBA ring

Parameters	Values
Hor. emit. (pm)	31
Natural chrom. (x/y)	-125/-108
Tune (x/y)	73.19/28.62
Energy spread	$7.1 \times 10^{-4}$
Damp. partition (x/y/s)	2.0/1.0/1.0

A two-stage optimization has been implemented. First, the settings of the chromatic and harmonic sex-

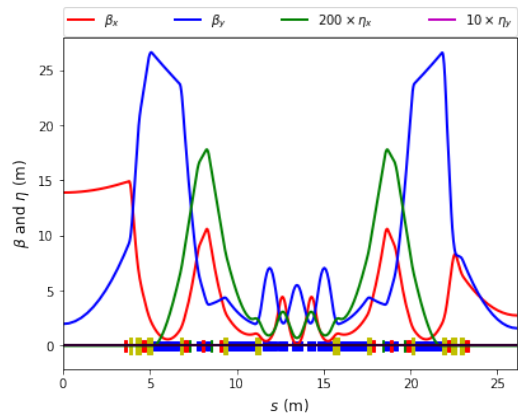


Figure 12. (Color) The linear optics and magnet layout for one cell of an ESRF-EBS type hybrid 7BA lattice. The red blocks represent sextupoles. Six chromatic sextupoles grouped into five families inside two dispersive bumps are used to correct the chromaticity with three extra degrees of freedom. Four harmonic sextupoles and four dispersive octupoles (green blocks) are also available for nonlinear dynamics optimization.

tupoles were optimized to correct the chromaticities, to minimize the fluctuations of the Courant-Snyder actions, and to maximize the ratio of the two leading frequency components. After this procedure, four octupoles inside the dispersive bumps were optimized to further minimize these objectives. The resulting DA is shown in Fig. 13.

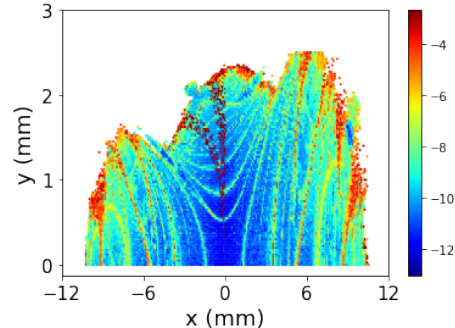


Figure 13. (Color) DA of the MBA lattice in the transverse  $x - y$  plane colored with the tune diffusion rate.

The MBA lattice was found to be more challenging than the DBA lattice in constructing QIs. The Courant-Snyder actions have larger fluctuations after optimization, especially in the vertical plane, as illustrated in Figs. 14 and 15. Nevertheless, particle orbits are still confined to tori in the horizontal plane, as seen in Fig. 16. More importantly, a large amplitude-dependent tune-spread is observed within the tune footprint of the stable DA, as shown in Fig. 17.

At large amplitudes, the trajectories in the vertical phase space significantly deviate from the Courant-Snyder ellipse (Fig. 16). However, this does not necessar-



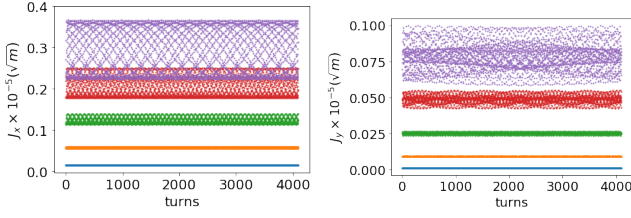


Figure 14. (Color) Evolution of  $J_{x,y}$  in the MBA lattice starting from 5 distinct initial conditions in the horizontal (left) and vertical (right) planes.

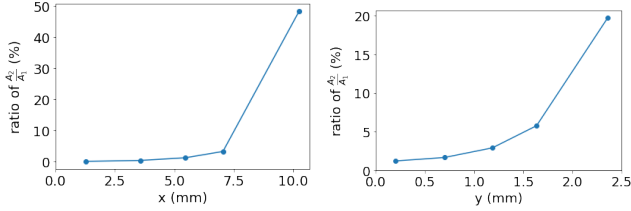


Figure 15. The ratio of the two leading NAFF frequencies for the MBA lattice in the horizontal (left) and vertical (right) planes.

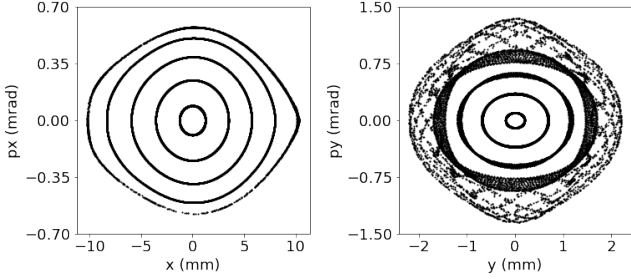


Figure 16. Simulated trajectories of the MBA lattice in the horizontal (left) and vertical (right) phase space. The vertical trajectories begin to smear out from thin tori gradually, but some patterns are visible.

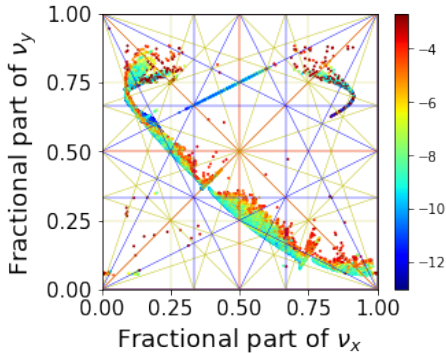


Figure 17. (Color) A large amplitude-dependent tune-spread is observed in the MBA lattice constructed with QIs.

ily indicate that the tori are broken, as the 2D projection of 4D tori are observed. A more detailed analysis, for ex-

ample, expanding the QI expression to high order polynomials for large-amplitude orbits in the vertical plane might be considered needed.

## V. DEPENDENCE ON LATTICE LOCATION

In the previous examples, the optimization procedure of Sect. II was performed using tracking data at a specific lattice location, e.g., at the center of the straight section. Here, the orbits lie on invariant tori that are nearly circular when projected into the  $\bar{x} - \bar{p}_x$  and  $\bar{y} - \bar{p}_y$  planes. However, it is not surprising to observe that the invariant tori are distorted at other locations in the lattice. Figure 18 shows an example of distorted tori observed at a location inside an achromat of the NSLS-II DBA lattice. The one-cell map behaves like an “optical anastigmat”, which has circular tori only at the periodic locations, i.e., its entrance and exit. Elsewhere in the lattice, distorted (perhaps broken) tori can be observed.

## VI. DECOHERENCE DUE TO NONLINEARITY

At the IOTA ring, its large amplitude-dependent tune-spread was found to provide a stabilization mechanism due to improved Landau damping [24]. Since constructed lattices with QI also provide a large nonlinear amplitude detuning, we used the DBA lattice to implement a 4-dimensional multi-particle simulation to illustrate this nonlinearity. A large tune spread due to the nonlinearity of betatron oscillations can be indirectly observed by kicking a bunched beam transversely [25]. A Gaussian distributed bunched beam was simulated by 4,000 macroparticles with the horizontal beam size as  $\sigma_x$ . After being kicked to an amplitude  $Z = a\sigma_x$ , the beam centroid will decay to the origin as the betatron phases of particles at different amplitudes decohere, which is described by the decoherence factor,

$$A(N) = \frac{1}{1 + \theta^2} \exp \left[ -\frac{Z^2}{2} \frac{\theta}{1 + \theta^2} \right], \quad (6)$$

here,  $N$  is the number of turns after being kicked,  $\theta = 4\pi\mu N$ , and  $\mu(Z) = \frac{d\nu}{da^2}$  is the local amplitude detuning coefficient at  $Z$ . The phase space distribution of the beam filaments from a localized bunch to an annulus which occupies all betatron phases (see Fig. 19), and the observed centroid of the beam will show a decaying oscillation (see Fig. 20). From the decoherence factor curve (the red line in Fig. 20), the local tune-shift-with-amplitude coefficient can be determined and confirmed with the spectrum analysis of the single particle tracking data in Fig. 21.

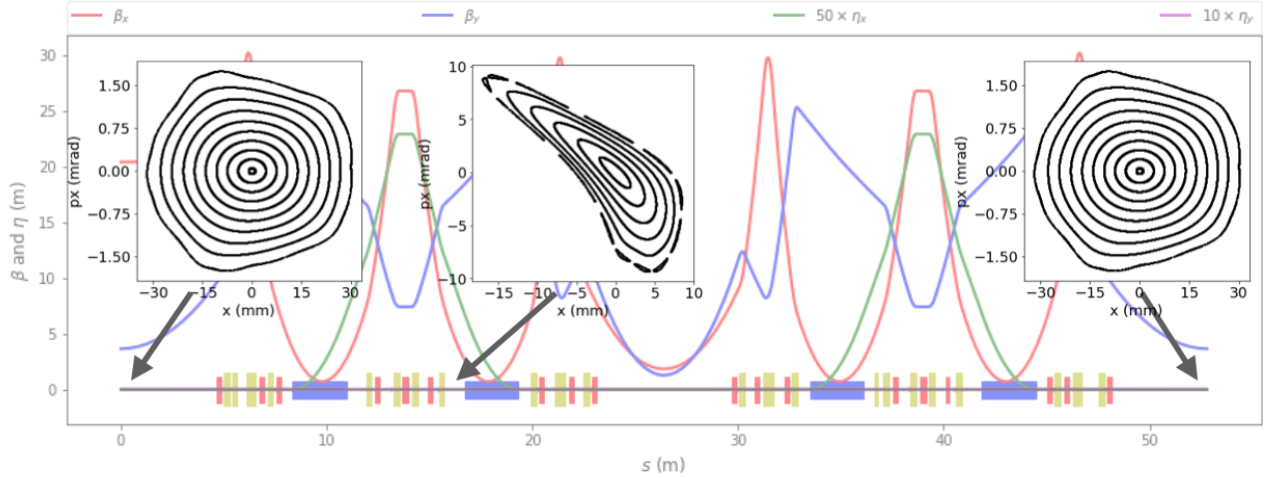


Figure 18. Tori are near-circular only when observed at the long straight section, but could be distorted at other locations.

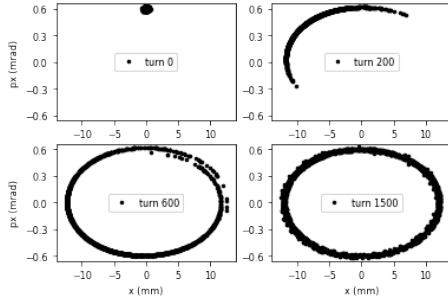


Figure 19. After being kicked, the phase space distribution of the beam spreads from a localized bunch to an annulus which occupies all betatron phases eventually.

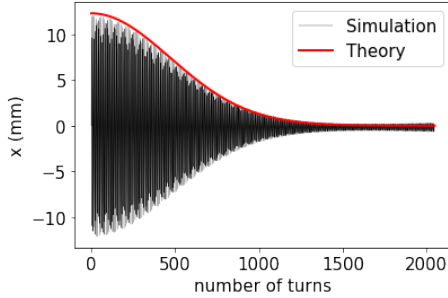


Figure 20. (Color) After being kicked, the centroid of the beam will show a decaying oscillation. The red line is known as the decoherence factor in Eq. (6), and can be used to determine the local amplitude detuning coefficient  $\mu$ .

## VII. DISCUSSION AND SUMMARY

So far, only the on-momentum particle motion has been described. In practice, a sufficient off-momentum acceptance is required as well. In the two exam-

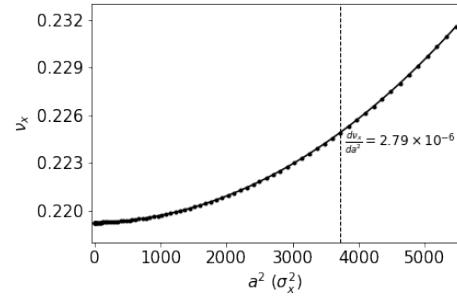


Figure 21. The tune-shift-with-amplitude curve obtained by the single particle tracking simulation. The horizontal axis is normalized with the unit of the square of beam size  $\sigma_x^2$ . The local slope at the kicked beam amplitude (at the dashed line) agrees with the decoherence factor computed from the centroid motion in Fig. 20.

ples of Sect. III-IV, on-momentum lattices were constructed with two quasi-invariants, and then the off-momentum acceptances were checked with tracking simulations. Both lattices were found to have sufficient local momentum aperture for the Touschek lifetime as shown in Fig. 22. In case the momentum acceptance also needs to be optimized, the method can be expanded to include a set of off-momentum particles. For an off-momentum particle, the dispersive reference orbit needs to be computed first, and then the Courant-Snyder actions  $J_{x,y}$  in (4) need to be computed using the momentum-dependent Twiss parameters  $\alpha(\delta, K_i)$ ,  $\beta(\delta, K_i)$  and  $\gamma(\delta, K_i)$  in Eq. (5). Note that the momentum-dependent Twiss parameters depend on the nonlinear magnets' excitation values  $K_i$ . For a given nonlinear magnet setting, the reference closed orbit and the corresponding momentum-dependent Twiss parameters need to be updated prior to the normalization.

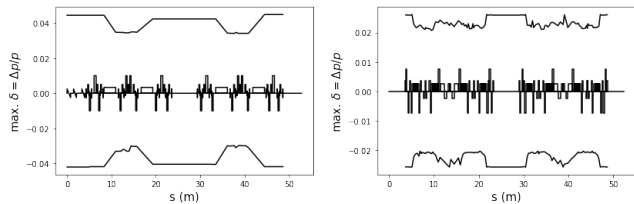


Figure 22. Local momentum aperture of one supercell (including two mirror symmetric cells) for the constructed DBA (left) and MBA (right) lattices.

In this paper, we demonstrated that a conventional DBA or MBA lattice can be re-tuned to possess two approximate invariants by optimizing the settings of only the sextupoles and octupoles. While the resulting DA is large (but finite), most particle trajectories are regular and confined to tori, and the amplitude-dependent betatron tunes are well-defined and stable. Like the lattice of the IOTA ring, a large nonlinear tune-spread exists that can provide enhanced Landau damping. The stop-band widths are observed narrow while the tune crosses low order resonance lines.

## ACKNOWLEDGMENTS

We would like to thank L-H. Yu (BNL), M. Borland, R. Lindberg, Y. Sun (ANL) and Y. Hao (MSU), E. Stern, A. Valishev, A. Romanov (FNAL), N. Kuklev (UChicago), G. Xu (IHEP) for the stimulating and collaborative discussions. This research is supported by the U.S. Department of Energy under Contract No. DE-SC0012704 (BNL) and DE-AC02-05CH11231 (LBNL). Co-authors from LBNL would like to acknowledge the support from the U.S. DOE Early Career Research Program under the Office of High Energy Physics.

## APPENDIX: ALTERNATIVE OPTIMIZATION SCHEMES

We can add additional terms to the Courant-Snyder actions  $J_{x,y}$  in (4), and use these in the optimization procedure described in Sect. II, in order to construct a lattice with more complicated quasi-invariants. Here, we demonstrate this method by modifying the quasi-invariant  $J_x$  to obtain triangle-shaped tori,

$$\begin{aligned} J_x(\phi_x) &= J_0 + \Delta J_x(\phi_x) \\ &= J_0 \left\{ 1 + \delta \sin \left[ n \left( \phi_x - \frac{\pi}{2n} \right) \right] \right\}, \end{aligned} \quad (7)$$

where  $\delta = \frac{\Delta J_x}{J_0}$  and  $n = 3$ . The phase dependence (top) of  $J_x$  and the expected torus in the horizontal phase space (bottom) are illustrated in Fig. 23.

After modifying the optimization procedure to minimize the fluctuations of (7) in the DBA lattice, a new set

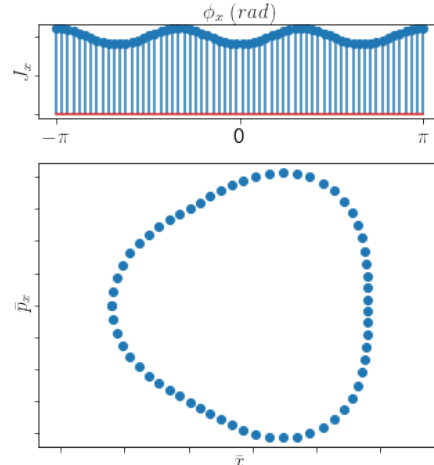


Figure 23. (Color) Adding a periodic phase dependence (top) to the action  $J_x$  can reshape a circular torus into a triangle-shaped one (bottom).

of sextupole settings were obtained. Tracking simulation confirmed that the tori have been reshaped as expected (Fig. 24). Such a phase space manipulation technique might be useful when a non-symmetric DA is desired. For example, a slightly larger inboard DA might be preferred to capture off-axis injected beam from that region.

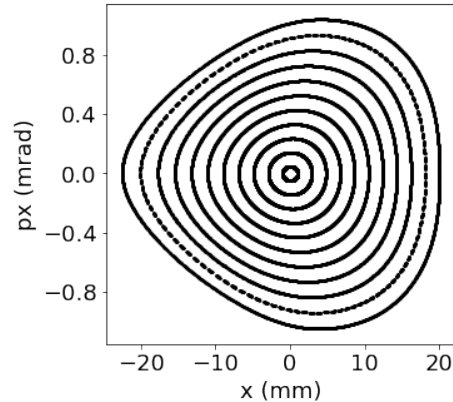


Figure 24. Particle trajectories are confined to triangle-shaped tori, as confirmed by the tracking simulation. A non-symmetric DA can be obtained with this technique.

However, the phase dependence of (7) can introduce additional frequency components into the betatron spectrum. For example, a weak component sitting near  $1/3$  is visible through the NAFF analysis in Fig. 25. If the betatron phase dependence is weak, it does not appear to spoil the overall performance of the nonlinear lattice. Note that the triangle-shaped tori are not caused by the betatron tune's approaching a third-order resonance. As seen in Fig. 25, the main betatron tune is around 0.22, and still far away from  $1/3$ .



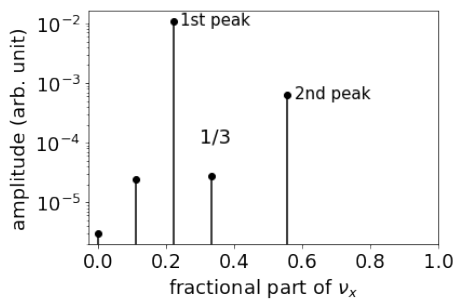


Figure 25. A weak  $1/3$  component is visible when a triangle-shaped modulation is added on a torus. The dominant tune is still around 0.22. The tori are distorted into triangle shapes, but not because the main tune is approaching the third order resonance.

- 
- [1] Sergey Antipov, Daniel Broemmelsiek, David Bruhwiler, Dean Edstrom, Elvin Harms, Valery Lebedev, Jerry Leibfritz, Sergei Nagaitsev, Chong-Shik Park, Henryk Piekarczyk, *et al.*, “IOTA (integrable optics test accelerator): facility and experimental beam physics program,” *Journal of Instrumentation* **12**, T03002 (2017).
  - [2] V Danilov, “Practical solutions for nonlinear accelerator lattice with stable nearly regular motion,” *Physical Review Special Topics-Accelerators and Beams* **11**, 114001 (2008).
  - [3] V Danilov and S Nagaitsev, “Nonlinear accelerator lattices with one and two analytic invariants,” *Physical Review Special Topics-Accelerators and Beams* **13**, 084002 (2010).
  - [4] K Ruisard, HB Komkov, B Beaudoin, I Haber, D Matthew, and T Koeth, “Single-invariant nonlinear optics for a small electron recirculator,” *Physical Review Accelerators and Beams* **22**, 041601 (2019).
  - [5] Alex J Dragt, “Lie methods for nonlinear dynamics with applications to accelerator physics,” unpublished (2011).
  - [6] Alexander Wu Chao, *Physics of collective beam instabilities in high energy accelerators* (Wiley, 1993).
  - [7] Eric Stern, *Suppression of Instabilities Generated by an Anti-Damper With a Nonlinear Magnetic Element in IOTA*, Tech. Rep. (Fermi National Accelerator Lab.(FNAL), Batavia, IL (United States), 2018).
  - [8] Li Hua Yu, “Analysis of nonlinear dynamics by square matrix method,” *Physical Review Accelerators and Beams* **20**, 034001 (2017).
  - [9] M. Borland, personal communication.
  - [10] Yipeng Sun and Michael Borland, “Comparison of Nonlinear Dynamics Optimization Methods for APS-U,” in *2nd North American Particle Accelerator Conference* (2017) p. WEPOB15.
  - [11] Joseph Liouville, “Note sur l’intégration des équations différentielles de la dynamique, présentée au bureau des longitudes le 29 juin 1853.” *Journal de Mathématiques pures et appliquées*, 137–138 (1855).
  - [12] VI Arnold, “Mathematical Methods of Classical Mechanics, Springer-Verlag, Berlin and New York, 1989,” .
  - [13] E.D Courant and H.S Snyder, “Theory of the alternating-gradient synchrotron,” *Annals of Physics* **3**, 1 – 48 (1958).
  - [14] H. Yoshida, “Construction of higher order symplectic integrators,” *Phys. Lett.* **A150**, 262–268 (1990).
  - [15] A W Chao, *Lecture Notes on Topics in Accelerator Physics* (SLAC, Stanford, CA, 2002).
  - [16] J. Laskar, “Frequency Map Analysis and Particle Accelerators,” in *20th Particle Accelerator Conference (PAC 03)* (2003) p. 378.
  - [17] Kalyanmoy Deb, *Multi-Objective Optimization Using Evolutionary Algorithms* (Wiley, 2001).
  - [18] DA Edwards and LC Teng, “Parametrization of linear coupled motion in periodic systems,” *IEEE Transactions on nuclear science* **20**, 885–888 (1973).
  - [19] BNL, <https://www.bnl.gov/nslls2/project/PDR/>.
  - [20] M. Borland, “elegant: A Flexible SDDS-Compliant Code for Accelerator Simulation,” in *Advanced Photon Source LS-287* (2000).
  - [21] L Farvacque, N Carmignani, J Chavanne, A Franchi, G Le Bec, S Liuzzo, B Nash, T Perron, P Raimondi, *et al.*, “A low-emittance lattice for the ESRF,” *Proc. IPAC’13*, 79–81 (2013).
  - [22] B Riemann and A Streun, “Low emittance lattice design from first principles: Reverse bending and longitudinal gradient bends,” *Physical Review Accelerators and Beams* **22**, 021601 (2019).
  - [23] Tong Zhang and Xiaobiao Huang, “Numerical optimization of a low emittance lattice cell,” *Nuclear Instruments and Methods in Physics Research Section A: Accelerators, Spectrometers, Detectors and Associated Equipment* **923**, 55–63 (2019).
  - [24] Sergey Antipov, Sergei Nagaitsev, *et al.*, “Single-particle dynamics in a nonlinear accelerator lattice: attaining a large tune spread with octupoles in iota,” *Journal of Instrumentation* **12**, P04008 (2017).
  - [25] R. E. Meller, A. W. Chao, J. M. Peterson, Stephen G. Peggs, and M. Furman, “Decoherence of Kicked Beams,” *SSC-N-360* (1987).